Journal of Computational Physics 228 (2009) 2468–2479

Contents lists available at ScienceDirect

Journal of Computational Physics

journal homepage: www.elsevier.com/locate/jcp

On accuracy and performance of high-order finite volume methods in local mean energy model of non-thermal plasmas

M. Davoudabadi [a], J.S. Shrimpton [b], F. Mashayek [a,*]

[a] Department of Mechanical and Industrial Engineering, University of Illinois at Chicago, 842 West Taylor Street, Chicago, IL 60607, USA
[b] Energy Technology Research Group, School of Engineering Sciences, University of Southampton, Highfield Campus, Southampton S017 1BJ, UK

ARTICLE INFO

Article history:
Received 24 May 2008
Received in revised form 28 November 2008
Accepted 4 December 2008
Available online 25 December 2008

Keywords:
High-order simulations
Finite volume method
Non-equilibrium plasma
Plasma discharge model

ABSTRACT

In this paper, a high-order finite volume method is employed to solve the local energy approximation model equations for a radio-frequency plasma discharge in a one-dimensional geometry. The so called deferred correction technique, along with high-order Lagrange polynomials, is used to calculate the convection and diffusion fluxes. Temporal discretization is performed using backward difference schemes of first and second orders. Extensive numerical experiments are carried out to evaluate the order and level of accuracy as well as computational efficiency of the various methods implemented in the work. These tests exhibit global convergence rate of up to fourth order for the spatial error, and of up to second order for the temporal error.

1. Introduction

Over the past few decades, considerable effort has been devoted to modeling non-thermal RF plasma discharges typical of those used in plasma processing of microelectronics devices [1] as well as coating of submicron-sized particles [2]. The deterministic continuum approach has proved to be computationally efficient in resolving various disparate length and time scales involved in the process. Gogolides and Sawin [3] have presented fundamental assumptions and a detailed derivation of the so called 'local energy approximation model' equations from the first three moments of the Boltzmann equation. In such a second-order hydrodynamic model [4–8,3,9–20], the electron energy is conserved, and the ionization rate coefficient is an empirical function of the local mean electron energy. This is particularly useful in the simulation of plasma flows where full chemistry of the carrier gas is considered (see [17,21,20,22]). The first-order 'local field approximation model' [23–37], on the other hand, is characterized by dependence of ionization on electric field. In this model, Townsend's first ionization coefficient is described by empirical expressions for the noble background gases [38].

RF and DC plasmas have been simulated with a variety of spatial discretization methods. These include first-order upwind [26,39,10,35,36], central difference [40], Scharfetter–Gummel [24,25,12,41,16,17,21] finite difference schemes, and the finite element method [4–6,11]. Spectral methods are promoted as more appropriate and include a spectral element [42] and a Chebyshev-collocation spectral (with single domain) scheme [19].

Balance equations for variables within a finite volume framework are naturally conservative and have simple physical interpretation. The goal of the present study comprises implementation of a semi-implicit, high-order finite volume method in solving the local mean energy model equations, and comparison of the accuracy and performance of various spatial and temporal methods within this framework. To the best of the authors knowledge, there is no report in the literature on this issue to date.

* Corresponding author. Tel.: +1 312 996 1154.
E-mail address: mashayek@uic.edu (F. Mashayek).

0021-9991/$ - see front matter © 2008 Elsevier Inc. All rights reserved.
doi:10.1016/j.jcp.2008.12.015

We use the deferred correction method [43,44] to discretize the diffusion and electrical convection terms. In this approach, to keep the size of the computational molecule small, a low-order method is used to implicitly discretize the fluxes, while the difference between the explicitly computed high- and low-order flux approximation is added as a source term. At convergence of the solution for the transport equation, the low-order approximation terms drop out and the high-order solution is retrieved. As the low-order implicit scheme, we employ first-order upwind (or central difference) for the electrical convective flux and central difference for the diffusive flux. Various explicit high-order fluxes are calculated from Lagrange polynomials. The gradient fields are also defined using a range of accuracy orders, and spatial integrations are performed using a fourth-order approximation. Boundary conditions are treated with up to fourth-order accuracy. Here, we restrict our geometry to a Cartesian one-dimensional infinite parallel plate. Our long term aim, however, is to use this 'benchmarking' study to produce a code that can both efficiently and accurately simulate RF plasma physics in three-dimensional complex geometries. In doing so, we will systematically examine the numerical treatment of different terms in the transport equations and establish the viability and the accuracy of our method against more sophisticated spectral methods, since it is suggested that the accurate solution of the local mean energy model equations requires very high-order spatial descritization [42,40].

It is noted here that under the same operating conditions and parameters and as long as the machine accuracy or the computational time is not an obstacle, all of the above-mentioned numerical strategies give the same solution at mesh convergence, regardless of the numerical treatment of convection, diffusion, and temporal 'flux', and the way in which the gradient fields or spatial integrations are estimated. However, as will be discussed later, the rate of convergence to a mesh independent solution is dependent upon the spatial flux scheme order and spatial descritization, and also temporal flux order and temporal descritization, whose performance we feel has not been given sufficient prominence in the literature.

2. Plasma model equations and non-dimensionalization

The local mean energy approximation model in dimensional form consists of the following set of conservation equations [4,11,12,16]:

$$\frac{\partial n_{i,e}^*}{\partial t^*} + \vec{\nabla}^* \cdot \vec{\Gamma}_{i,e}^* = k_i^* n_e^* n_n^*, \tag{1}$$

$$\frac{\partial \omega_e^*}{\partial t^*} + \vec{\nabla}^* \cdot \vec{\Gamma}_{\omega_e}^* = -e\vec{\Gamma}_e^* \cdot \vec{E}^* - k_i^* n_e^* n_n^* H_i^*, \tag{2}$$

$$\nabla^{*2}\phi^* = \frac{e}{\epsilon_0}(n_e^* - n_i^*), \tag{3}$$

where the flux expressions are defined as,

$$\vec{\Gamma}_i^* = +\mu_i^* \vec{E}^* n_i^* - D_i^* \vec{\nabla}^* n_i^*, \tag{4}$$

$$\vec{\Gamma}_e^* = -\mu_e^* \vec{E}^* n_e^* - D_e^* \vec{\nabla}^* n_e^*, \tag{5}$$

$$\vec{\Gamma}_{\omega_e}^* = \frac{5}{3}\left(-\mu_e^* \vec{E}^* \omega_e^* - D_e^* \vec{\nabla}^* \omega_e^*\right), \tag{6}$$

and other subsidiary equation being,

$$\vec{E}^* = -\vec{\nabla}^* \phi^*. \tag{7}$$

In the above set of equations, $n_{i,e}^*$ refers to ion, electron number density, and ω_e^* denotes mean electron energy density. $\vec{\Gamma}_{i,e}^*$ represents ion, electron fluxes, and $\vec{\Gamma}_{\omega_e}^*$ indicates mean electron energy density flux. k_i^* is the ionization rate coefficient, while H_i^* designates ionization energy. $n_n^* = P/k_B T_n$ gives the neutral number density, with P, k_B, and T_n denoting the reactor pressure, Boltzmann constant, and neutral species temperature, respectively. The electric potential is represented by ϕ^* and the electric field by $\vec{E}^*$. The elementary charge is shown by e, and ϵ_0 is permittivity of free space. Finally, $\mu_{e,i}^*$ and $D_{e,i}^*$ represent electron, ion mobility and diffusion coefficients, respectively.

We consider a parallel plate RF glow discharge plasma reactor as shown in Fig. 1. Thus, for our one-dimensional case, $\vec{\nabla}^* \equiv d/dx^*$, $\vec{\Gamma}_{i,e}^* \equiv \vec{\Gamma}_{x_{i,e}}^* \equiv \Gamma_{i,e}^*$, $\nabla^{*2} \equiv d^2/dx^{*2}$, and $\vec{E}^* \equiv E_x^* = E^*$. The values of transport coefficients and various parameters of the argon discharge used in the present simulations are tabulated in Table 1. We use x_0, ϕ_0, and μ_0 as the characteristic dimensional scales for length, voltage, and mobility, respectively. Noting that ion and electron mobility and diffusion coefficients are constant, the following dimensional scales, generically denoted by φ_0, are then derived as:

$$n_0 = \frac{\epsilon_0 \phi_0}{e x_0^2}, \quad D_0 = \mu_0 \phi_0$$

$$\omega_0 = e\phi_0 n_0, \quad t_0 = \frac{x_0^2}{D_0}$$

$$H_{i0} = \omega_0 n_0, \quad k_{i0} = \frac{1}{n_0 t_0}$$

$$E_0 = \frac{\phi_0}{x_0}, \quad f_0 = \frac{1}{t_0}.$$

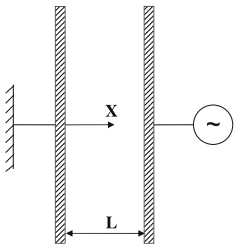

Fig. 1. Schematic of the problem.

Table 1
Transport coefficients and parameters used in the simulations, from Refs. [12,19].

Parameter	Value
$\mu_e^* P$	$30.0\ \left(\frac{m^2}{Vs}\text{torr}\right)$
$D_e^* P$	$120.0\ \left(\frac{m^2}{s}\text{torr}\right)$
$\mu_i^* P$	$0.14\ \left(\frac{m^2}{Vs}\text{torr}\right)$
$D_i^* P$	$4.0\times10^{-3}\ \left(\frac{m^2}{s}\text{torr}\right)$
k_i^*	$\begin{cases} 0 & \frac{\omega_e^*}{en_e^*} \leqslant 5.3\ \text{eV} \\ 8.7\times10^{-15}\left(\frac{\omega_e^*}{en_e^*}-5.3\right)\exp\left(-4.9/\sqrt{\frac{\omega_e^*}{en_e^*}-5.3}\right)\ \left(\frac{m^3}{s}\right) & \frac{\omega_e^*}{en_e^*} > 5.3\text{eV} \end{cases}$
H_i^*	$15.578\times e$ (J)
f^*	13.56 (MHz)
L	0.02 (m)
P	1 (torr)
$T_i = T_n$	293 (K)
ϕ_{rf}	40 (V)

For any dimensional variable, φ^*, its non-dimensional counterpart is defined as $\varphi = \varphi^*/\varphi_0$, and this leads to the following non-dimensional equations, valid also for DC plasma discharges:

$$\frac{\partial n_i}{\partial t} + \mu_i \frac{\partial}{\partial x}(E n_i) = D_i \frac{\partial^2 n_i}{\partial x^2} + k_i n_e n_n, \tag{8}$$

$$\frac{\partial n_e}{\partial t} - \mu_e \frac{\partial}{\partial x}(E n_e) = D_e \frac{\partial^2 n_e}{\partial x^2} + k_i n_e n_n, \tag{9}$$

$$\frac{\partial \omega_e}{\partial t} - \frac{5}{3}\mu_e \frac{\partial}{\partial x}(E\omega_e) = \frac{5}{3} D_e \frac{\partial^2 \omega_e}{\partial x^2} + \mu_e n_e E^2 + D_e E \frac{\partial n_e}{\partial x} - k_i n_e n_n H_i, \tag{10}$$

$$0 = \frac{\partial^2 \phi}{\partial x^2} + (n_i - n_e), \tag{11}$$

$$E = -\frac{\partial \phi}{\partial x}. \tag{12}$$

Eqs. (8)–(10) form a set of three convection–diffusion transport differential equations, while Eq. (12) couples them to Poisson's Eq. (11) for electric potential. We choose the characteristic scales $x_0 = L$, the inter-electrode gap, $\phi_0 = \phi_{rf}$, the amplitude of the applied RF voltage with excitation frequency f^*, and $\mu_0 = \mu_e^*$.

Although more realistic boundary conditions like those in [37,45] can be readily implemented, we use the conditions of Table 2 for the sake of direct comparison of our results with those of Lin and Adomaitis [19].

Table 2
Boundary conditions on primary variables.

Boundary	Condition on n_i	Condition on n_e	Condition on ω_e	Condition on ϕ
$x = 0$	$\frac{\partial n_i}{\partial x} = 0$	$n_e = 0$	$\omega_e = 0$	$\phi = 0$
$x = 1$	$\frac{\partial n_i}{\partial x} = 0$	$n_e = 0$	$\omega_e = 0$	$\phi = \sin(2\pi f t)$

3. Notes concerning the finite volume method implementation

Take as an example the non-dimensional ion transport equation which has the following integral form:

$$\int_{\Omega} \frac{\partial n_i}{\partial t} d\Omega + \mu_i \oint_S E n_i dS = D_i \oint_S \frac{\partial n_i}{\partial x} dS + \int_{\Omega} k_i n_e n_n d\Omega, \tag{13}$$

where Ω denotes the volume of the control volume (CV), and S is the surface enclosing the CV. To perform the integration of the temporal and the source terms over a CV, P in Fig. 2, we first pass a quadratic polynomial, as the shape function assumed within the CV, through the center points W, P, and E. Then, we integrate the resulting polynomial from the west to the east face of the CV. Such an approximation is of fourth-order accuracy, whereas the conventional mid-point rule possesses an accuracy of second-order [44]. The electrical convection term, in the context of the finite volume method, requires specific mention. In order to create a linearized algebraic tridiagonal equation set, with a matrix structure of the form

$$(A_W + A_E) n_i|_P = A_P n_i|_P = A_W n_i|_W + A_E n_i|_E + Q_P, \tag{14}$$

we make use of the Poisson equation in the integral form,

$$\oint_S E dS = \int_{\Omega} (n_i - n_e) d\Omega, \tag{15}$$

as a continuity equation. Such a matrix structure, with A_P equal to sum of all neighbor coefficients and $A_E, A_W \geqslant 0$, characterizes all conservative schemes, ensuring that a uniform field satisfies the discretized homogeneous equation. Moreover, it enhances the diagonal dominance of the matrix A. Multiplying the above equation by $\mu_i n_i$, and subtracting the result from Eq. (13) gives

$$\int_{\Omega} \frac{\partial n_i}{\partial t} d\Omega + \mu_i \oint_S E n_i dS - \mu_i n_i \oint_S E dS = D_i \oint_S \frac{\partial n_i}{\partial x} dS + \int_{\Omega} k_i n_e n_n d\Omega + \mu_i n_i \int_{\Omega} (n_e - n_i) d\Omega. \tag{16}$$

Using compass notation as defined in Fig. 2, the discrete approximation to the convection related terms in the above equation is

$$-\mu_i n_i \oint_S E dS + \mu_i \oint_S E n_i dS - \mu_i n_i \int_{\Omega} (n_e - n_i) d\Omega \simeq (F|_w - F|_e) n_i|_P - F|_w n_i|_w + F|_e n_i|_e - \mu_i n_i|_P \int_{\Omega} (n_e - n_i) d\Omega, \tag{17}$$

where $F|_w$ and $F|_e$ at the west and the east cell faces are defined, respectively, as

$$F|_w = \mu_i (SE)|_w, \qquad F|_e = \mu_i (SE)|_e,$$

with S denoting the cell surface area.

The face coefficients ($F|_e$ and $F|_w$) in Eq. (17) are computed by interpolating the cell center electric field values with a method that is consistent in order with that used to estimate the face values of the ion density field ($n_i|_w, n_i|_e$) with the minimum method order being two (central differencing). First term in the right-hand side (rhs) of Eq. (17) now resembles $A_P n_i|_P$ term in Eq. (14), and the face $n_i|_w, n_i|_e$ terms in Eq. (17) will be related to the nodal values (i.e. $n_i|_P$, $n_i|_E$, $n_i|_W$ of Eq. (14)) via some form of convection scheme. It is noted that the extra non-linear source term, i.e. the last term in the rhs of Eq. (17), may be linearized and added to the A_p coefficient thus improving the diagonal dominance of the matrix and the stability of the global algebraic numerical method.

The above technique is similarly applied in defining implicit convection coefficients and the required additional source terms for the other variables, i.e. n_e and ω_e.

High-order approximation of convective or diffusive fluxes is achieved using the deferred correction technique [43,44]. Taking as an example the ion density electrical convective flux, on the east face of a CV, P, we define the convective flux generally as

$$F|_e n_i|_e = \mu_i (SE)|_e n_i|_e \approx \mu_i (SE)|_e \{ n_i^{(i)}|_e + (n_i^{(h)}|_e - n_i^{(l)}|_e) \}, \tag{18}$$

where $n_i^{(i)}|_e$ is the implicit component and $(n_i^{(h)}|_e - n_i^{(l)}|_e)$ is an explicit 'deferred' correction, added to the flux term such that at convergence the net flux is that of the high-order scheme. Fluxes of order higher than two at the cell face are calculated using Lagrange polynomials [Eq. (19) in Appendix I] based on variable values at the nodes located on both sides of the cell. Close to the boundaries, the number of nodes on the left and the right are varied accordingly. Specific forms of $n_i^{(i)}|_e$ and $(n_i^{(h)}|_e - n_i^{(l)}|_e)$ are defined in Appendix I.

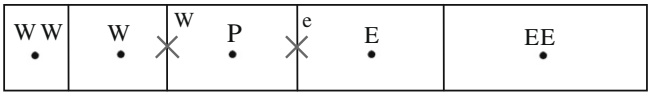

Fig. 2. Typical one-dimensional finite volume non-uniform mesh with compass notation.

Table 3
Temporal discretization schemes employed in the present study.

Order	$\frac{\partial n_i}{\partial t}$
1st	$\frac{n_i^{n+1} - n_i^n}{\Delta t}$
2nd	$\frac{3n_i^{n+1} - 4n_i^n + n_i^{n-1}}{2\Delta t}$

The diffusion fluxes are also evaluated using the same deferred correction approach,

$$\left.\frac{\partial n_i}{\partial x}\right|_e = \left.\left(\frac{\partial n_i}{\partial x}\right)^{(i)}\right|_e + \left\{\left.\left(\frac{\partial n_i}{\partial x}\right)^{(h)}\right|_e - \left.\left(\frac{\partial n_i}{\partial x}\right)^{(l)}\right|_e\right\}.$$

Here, the implicit component is approximated by a second-order central difference approximation

$$\left.\left(\frac{\partial n_i}{\partial x}\right)^{(i)}\right|_e = \frac{n_i|_E - n_i|_P}{x|_E - x|_P},$$

and the explicit term represents the difference between the explicit version of $\left(\frac{\partial n_i}{\partial x}\right)^{(i)}|_e$ and a higher-order differentiated Lagrange polynomial (Eq. (19) in Appendix I).

We also note that the gradient fields of all variables, particularly important for some of the source terms, may also be estimated using the same high-order gradient estimator. Furthermore, all the source terms are treated semi-implicitly and calculated based on the values of the variables and their gradients computed in the last internal iteration. Moreover, as demonstrated in Table 3, temporal discretization utilizes a first- or second-order backward difference scheme. Finally, boundary conditions with accuracy of up to fourth-order are implemented using one-sided difference methods. It is stressed that since arbitrarily high-order convection, diffusion, and gradient terms are already implemented in our code, higher orders than four in space are attainable by employing higher order spatial integration schemes (for the temporal and source terms), and higher order boundary conditions.

Discretization of the integral form of the system of Eqs. (8)–(11) leads to a system of coupled algebraic equations for the discrete variables defined at the cell centers. At each time step, these coupled equations are solved iteratively until the maximum (both in space and among the variables) error becomes less than a tolerance of 10^{-8}:

$$\max\left\{\frac{|\varphi_i^k - \varphi_i^{k-1}|}{1 + |\varphi_i^k|}\right\} < 10^{-8}, \quad 1 \leqslant i \leqslant N_{CV},$$

where superscripts k and $k-1$ denote the values of the generic variable φ at the current and previous iterations, respectively. Inside each inter-equation iteration, the low-cost Thomas algorithm [44] is used to solve tridiagonal system of the equations. Different initial conditions proved to give the same results. However, to perform an appropriate error analysis, all the test cases start from the same uniform initial condition for $t \leqslant 0$, with $n_i = n_e = 5 \times 10^{15}/n_0$ and $\omega_e = 5 \times 10^{15} \times e/\omega_0$.

4. Results and discussion

4.1. Overview of simulations and the test matrix

As mentioned in the introduction, the objective of the present study is to compare the accuracy and performance of the schemes treating the various terms involved in the local mean energy model equations. Parameters involved in such a study consist of spatial resolution (N_{CV}, total number of control volumes in the domain), temporal resolution (N_{ts}, number of time steps per RF cycle), time flux (tfds), convection flux (cfds), diffusion flux (dfds), and gradient field (gfds) discretization schemes. Types of convection schemes (cfds) are denoted as U (first-order upwind), CD (second-order central difference), and TVD (Superbee Total Variation Diminishing flux limiter [46]). In all these cases, interpolation of the cell center electric field to the cell face in order to calculate the cell face flux coefficients is performed using a second-order central difference. Where the index is numeric, this represents the order of the Lagrange polynomial used to interpolate node values to the face. For the diffusion flux (dfds) and the gradient field (gfds) numerical methods, the numerical index represents the order of the original Lagrange polynomial differentiated if dfds or gfds are greater than 2, otherwise pure implicit central differencing. The order of accuracy of the one-sided finite difference schemes through which the boundary conditions are approximated correspond to the index indicated by dfds and gfds.

Considering the six-dimensional parameter space, we define a test matrix comprising 27 tests as tabulated in Table 4. Tests 1–3, 4–6, 7–9, 10–12, 13–16, 17–19 investigate the effect of uniform mesh resolution and spatial scheme choice, whereas tests 20–22, and 23–26 concern with the effect of temporal resolution and scheme order for a highly resolved spatial domain. For all of the cases, errors of the instantaneous primary variables are calculated at the time point corresponding to the three quarters of the 250th cycle. For a generic variable φ, the following ℓ_1-norm of the relative error is used as a measure of accuracy:

Table 4
Spatial resolution (N_{CV}), temporal resolution (N_{ts}), numerical scheme, total CPU time (tct), last cycle CPU time (lct) and accuracy of test cases. tfds, cfds, dfds, and gfds denote time flux, convection flux, diffusion flux, and gradient field discretization schemes, respectively.

Case no.	N_{CV}	N_{ts}	tfds	cfds	dfds	gfds	tct (s)	lct (s)	ζ_{n_i}	ζ_{n_e}	ζ_{ω_e}	ζ_{ϕ}
1	200	80	2	U	1	1	815.0	3.5	1.28E−01	1.36E−01	1.35E−01	5.02E−01
2	400	80	2	U	1	1	1632.7	7.1	7.06E−02	7.33E−02	7.34E−02	1.18E−01
3	800	80	2	U	1	1	3303.9	14.5	3.90E−02	4.03E−02	4.03E−02	4.29E−02
4	200	80	2	CD	2	2	803.6	3.4	1.70E−01	1.76E−01	1.76E−01	3.25E−01
5	400	80	2	CD	2	2	1692.5	7.4	2.65E−02	2.75E−02	2.76E−02	5.16E−02
6	800	80	2	CD	2	2	3415.6	15.0	6.29E−03	6.53E−03	6.54E−03	1.19E−02
7	200	80	2	TVD	2	2	1013.8	4.3	1.74E−01	1.80E−01	1.80E−01	3.23E−01
8	400	80	2	TVD	2	2	2138.5	9.4	2.91E−02	3.01E−02	3.02E−02	5.21E−02
9	800	80	2	TVD	2	2	4320.6	19.0	7.02E−03	7.28E−03	7.29E−03	1.21E−02
10	200	80	2	U3	3	3	1214.6	5.4	1.07E−03	1.08E−03	1.08E−03	8.31E−04
11	400	80	2	U3	3	3	2403.4	10.5	9.00E−05	8.47E−05	8.71E−05	7.94E−05
12	800	80	2	U3	3	3	4801.8	21.1	1.11E−05	9.86E−06	1.02E−05	8.46E−06
13	200	80	2	U5	4	4	1252.4	5.5	2.34E−04	2.31E−04	2.28E−04	2.79E−04
14	400	80	2	U5	4	4	2478.7	10.9	1.42E−05	1.09E−05	1.07E−05	1.66E−05
15	800	80	2	U5	4	4	4953.5	21.7	1.29E−06	5.33E−07	5.27E−07	1.00E−06
16	6400	80	2	U5	4	4	39594.3	173.9				
17	200	80	2	CD5	4	4	1251.4	5.5	2.34E−04	2.31E−04	2.28E−04	2.79E−04
18	400	80	2	CD5	4	4	2479.7	10.8	1.42E−05	1.09E−05	1.07E−05	1.66E−05
19	800	80	2	CD5	4	4	4944.4	21.6	1.30E−06	5.38E−07	5.33E−07	1.00E−06
20	3200	40	1	U5	4	4	24833.5	111.5	4.65E−02	4.74E−02	4.82E−02	7.78E−03
21	3200	80	1	U5	4	4	26689.6	118.9	2.37E−02	2.42E−02	2.46E−02	4.00E−03
22	3200	160	1	U5	4	4	29586.5	129.2	1.20E−02	1.22E−02	1.24E−02	2.02E−03
23	3200	40	2	U5	4	4	18053.6	80.5	1.21E−02	1.24E−02	1.25E−02	1.37E−03
24	3200	80	2	U5	4	4	19736.7	86.8	2.90E−03	2.96E−03	2.99E−03	3.42E−04
25	3200	160	2	U5	4	4	22678.7	97.7	6.64E−04	6.78E−04	6.85E−04	7.90E−05
26	3200	640	2	U5	4	4	36807.5	152.7				
27	6400	640	2	U5	4	4	73862.5	305.4				

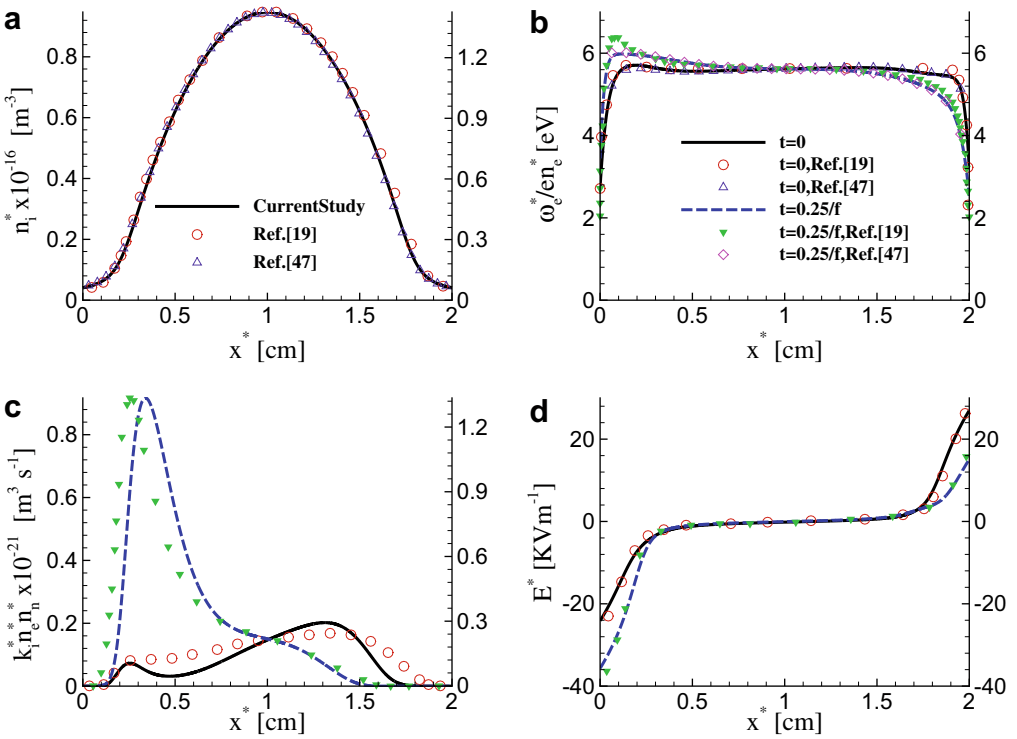

Fig. 3. Comparison of the quasi-steady-state results of the present study (solid lines and left vertical axes) with those of references [19] (symbols and right vertical axes) and [47] (symbols and left vertical axes). Spatial distribution of (a) ions concentration, (b) mean electron energy, (c) ionization rate, and (d) electric field at different times in the last RF cycle.

$$\zeta_\varphi = \frac{\sum_{i=1}^{N_{CV}} |\varphi_i^{exact} - \varphi_i|}{\sum_{i=1}^{N_{CV}} |\varphi_i^{exact}|},$$

where the prediction from tests 16 and 26 are deemed to be the spatially and temporally 'exact' solutions, respectively. Table 4 summarizes the accuracy and CPU time of these simulations which are performed on an L5310@1.60 GHz Intel Xeon CPU. "tct" therein reports the CPU time (in seconds) of the whole simulation from the first up to the 250th cycle, whereas "lct" represents the time (in seconds) taken to compute only the last RF cycle.

4.2. Comparisons with previous results

In Fig. 3, the results generated by setting $N_{CV} = 6400$, $N_{ts} = 640$, tfds = 2, cfds = U5, dfds = 4, and gfds = 4 (corresponding to case 27 in Table 4) are compared with those of references [19] and [47]. These parameters amount to our most highly resolved case in terms of spatial scheme order and resolution, and also temporal scheme order and resolution. Convergence of the whole system to the periodic, quasi-steady-state solution is ascertained to have been reached by running the simulation for 2000 cycles. At this stage, the relative difference in n_i at the central node, between two consecutive periods, at a quarter of the cycle is less than 10^{-6}. In comparison with the results of Lin and Adomaitis [19], relatively good qualitative agreement is observed in most of the x domain for all primary variables at the two times shown. Quantitatively, however, the peak number densities of ions (and electrons) in the results of Lin and Adomaitis lie ~50% higher as compared to those in our simulations. On the other hand, our results demonstrate excellent agreement, both quantitatively and qualitatively, when compared to those generated by Goedheer and coworkers [12,47] using the same parameters and conditions. It is emphasized that prior to this study, we implemented a finite difference method [36] where various convection discretization schemes such as first-order upwind, second-order upwind [48], central difference, and Scharfetter–Gummel along with central differencing for diffusion flux and backward Euler for temporal integration were employed. All of these methods predicted n_i and n_e which fall within 5% of the presented results of the current study.

Fig. 4 shows the general space-time character of the system. The powered electrode at $x^*/L = 1$ defines the voltage sine wave where ϕ = 40 V at $t^*/T = 0.25$. The ion density is not shown, but it is well-known that at a frequency of 13.56 MHz due to ions large mass per unit charge, this field is almost completely independent of time [24,36] and our results confirm this. The electron density and electron energy density fields (Fig. 4(a) and (b)) do have a small time as well as a space dependence.

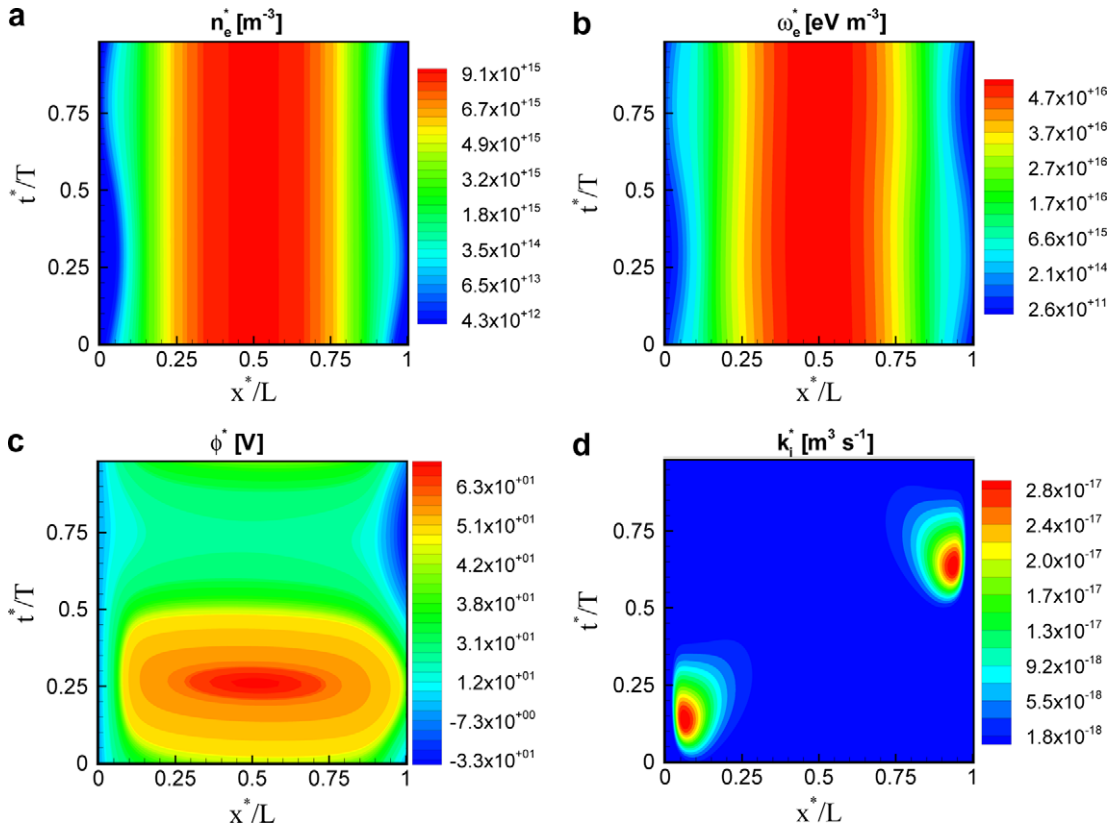

Fig. 4. The quasi-steady-state results corresponding to case 27 of the test matrix shown in Table 4. Space-time contours of (a) electron number density, (b) mean electron energy density, (c) electric potential, and (d) ionization rate coefficient.

However as Fig. 4(d) reveals, it is the variation of the ionization rate coefficient in space and time that is most striking, and where high spatial and temporal accuracy in the local $x - t$ space is most important.

4.3. Performance and accuracy

The accuracy versus cost of the choice of spatial scheme type may be assessed by comparing the errors of tests 2, 5, 8, 11, 14, 18, where $N_{CV} = 400$, $N_{ts} = 80$, and tfds = 2. The global scheme order rises from ~1 (test 2), ~2 (tests 5 and 8), to ~3 (test 11), and finally ~4 (tests 14 and 18). We observe a reduction in the magnitude of the error by more than three orders of magnitude for an increase in the total CPU time of ~50%. We can conclude from this that the deferred correction method, for higher order flux approximations is an efficient and robust method to obtain accurate solutions to RF plasma problems. In addition, with N_{ts}, tfds, cfds, dfds, and gfds kept constant (see cases 1–3, 4–6, 10–12, or 13–15 for instance), CPU time appears to be almost linearly proportional to the spatial resolution (N_{CV}) with a proportionality factor of ~1 (see also Fig. 5(e) and (f)).

Fig. 5(a)–(d) depicts as a function of N_{CV} the ℓ_1-norm of relative errors for various spatial schemes with a fixed time scheme (second-order) and time step size ($N_{ts} = 80$). In these plots, the order of accuracy of each scheme is denoted by the corresponding numerical legend, and is calculated as the negative of the slope of the line curve-fitted through points (ζ, N_{CV}). We show that the magnitude and order of the global error in all primary variables is controlled by the spatial scheme choice and mesh resolution, as defined by tests 1–19 of Table 4. It is also noteworthy in Fig. 5(a)–(d) that upwinding with 200 uniform cells results in $\zeta_{n_i} = 12.8\%$ and $\zeta_{n_e} = 13.6\%$ which correspond to an error in the maximum densities at the 250th cycle by as much as 8.5%. This figure suggests that to reach an accuracy of 10^{-4}, over ~750,000, 4800, 400, and 240 uniform cells are required when employing U, CD, U3, and U5/CD5, respectively. Corresponding CPU time for one cycle of such simulations would be over ~ 13,000, 90, 10, and 6 s.

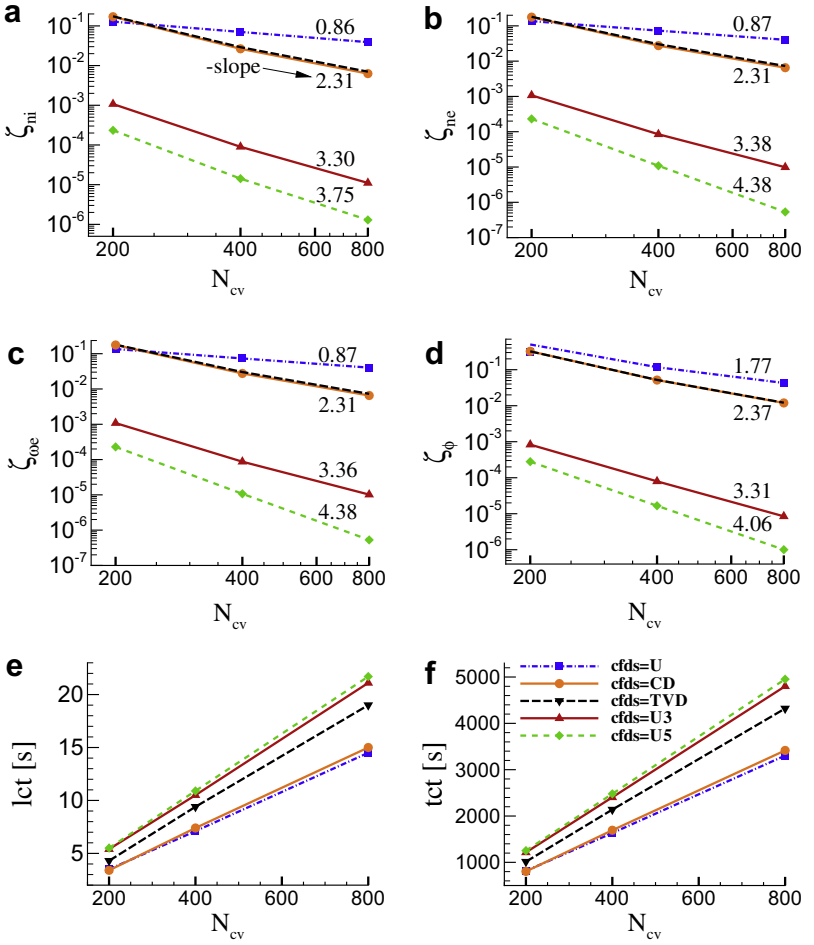

Fig. 5. (a)–(d) ℓ_1-norm of spatial relative errors, (e) last cycle CPU time (lct), and (f) total CPU time (tct) as a function of N_{CV} for various spatial schemes with tfds = 2 and $N_{ts} = 80$. Results are extracted at three quarters of the 250th cycle.

Fig. 5(e) and (f) shows, respectively, the last cycle CPU time (lct) and total CPU time (tct) for various spatial resolutions (N_{CV}) and discretization schemes. In these figures we observe that there is a considerable difference between the CPU times of U and CD, and those of U3 and U5. This trend is most likely because neither upwinding nor central differencing uses the deferred correction technique, whereas both U3 and U5 employ this technique in discretizing the convection and diffusion terms. CPU times of TVD scheme which uses deferred correction in only the convection term falls between the U/CD and U3/U5 cases. It is also remarkable that while cases 13–15 are only slightly slower than cases 10–12, cases 13–15 clearly exhibit significantly higher levels of accuracy.

As mentioned previously, in all of the cases, the spatial integration of the transient and volume source terms are performed using a fourth-order method. However, as apparent in Fig. 5(a)–(d), using lower order methods to interpolate the convective or diffusive fluxes, or to approximate the gradients or the boundary conditions yields a lower order error trend. Higher order trends of the global error are achieved when consistently applying higher order approximations to the various spatial terms. Moreover, we observe that the central difference and the Superbee TVD (a blended first-order upwind/second-order scheme) produce somewhat identical results in terms of the error trend and also the error magnitudes. This implies that the convected fields are all reasonably smooth and do not require the TVD limiter to activate. Among the various spatial schemes examined, the errors are minimal in magnitude and maximal in order in the case of the deferred correction with cfds = U5/CD5, dfds = 4, gfds = 4. Further, comparing tests 13–15 with 17–19 of Table 4 reveals that using central differencing instead of upwinding as the implicit convection flux discretizer has literally no effect on the global accuracy. Therefore, we confirm the deferred correction method provides a stable and accurate numerical method for finite volume/difference methods for RF plasmas and can produce significant savings on CPU time by using pre-computed interpolation polynomials.

Fig. 6(a)–(d) depicts the role of the time scheme order and the time step size, as defined by tests 20–26 of Table 4 upon the global accuracy. As with the spatial schemes, we observe with the temporal scheme a first-order global error trend for the first-order scheme and a second-order error trend for the second-order time scheme. This is somewhat surprising for the

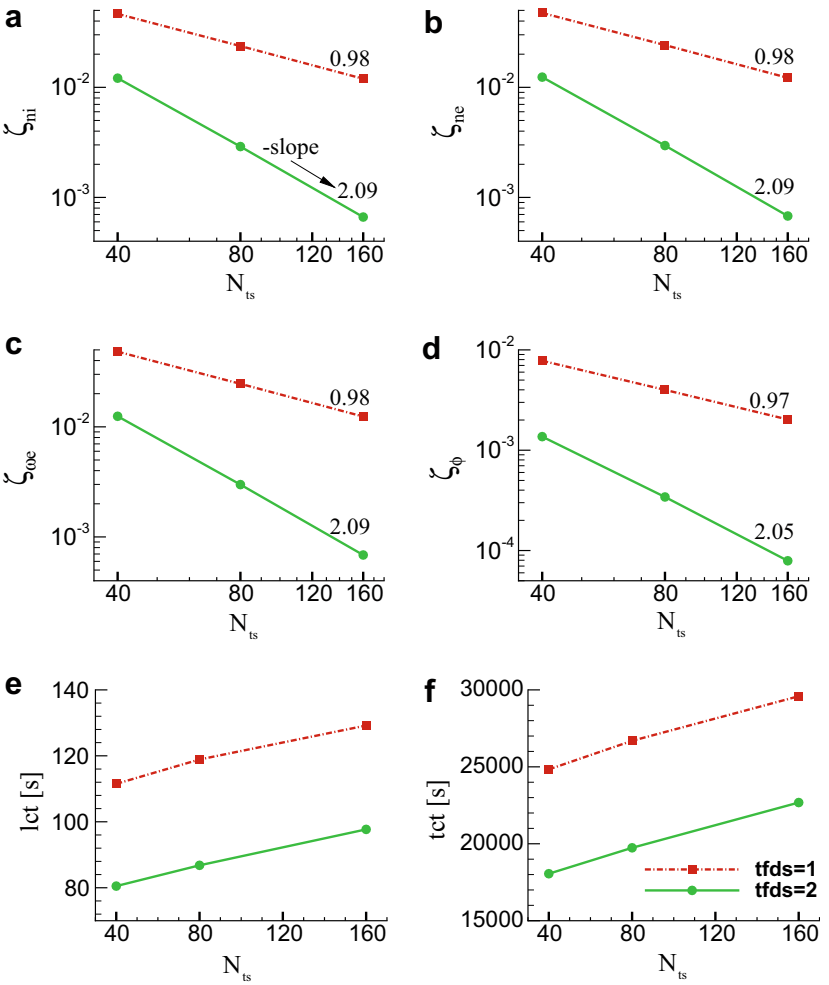

Fig. 6. (a)–(d) ℓ_1-norm of temporal relative errors, (e) last cycle CPU time (lct), and (f) total CPU time (tct) as a function of N_{ts} for various temporal schemes with cfds = U5, dfds = 4, gfds = 4, and $N_{CV} = 3200$. Results are extracted at three quarters of the 250th cycle.

Table 5
Total number of inter-equation iterations (N_{iter}) in the last cycle for various temporal flux discretization schemes (tfds) and number of time steps per cycle (N_{ts}).

Case no.	tfds	N_{ts}	N_{iter}	Case no.	tfds	N_{ts}	N_{iter}
20	1	40	4309	23	2	40	3061
21	1	80	4566	24	2	80	3302
22	1	160	4992	25	2	160	3713

voltage field, since no transient term exists in the Poisson equation, and implies that the equation is dominated by the ion and electron density source terms (whose fields are controlled by transient and convective transport). It is also noted the significantly increased accuracy the second-order scheme provides and this suggests two possibilities. First that further increase in time scheme order may bring further benefits in terms of accuracy and second that the use of higher order time scheme can bring significant CPU time savings by reducing the number of time steps required to resolve one RF cycle. For example, one to one comparison of tests 22 (with tfds = 1 and $N_{ts} = 160$) and 25 (with tfds = 2 and $N_{ts} = 160$) of Table 4 reveals that using a second-order time scheme leads to a decrease by 25% in CPU time and an increase by 18 times in level of temporal accuracy. Table 5 lists the total number of inter-equation iterations (N_{iter}) in the last cycle for various temporal flux discretization schemes (tfds) and number of time steps per cycle (N_{ts}). According to this table, in order to reach a value of 10^{-8} in the maximum change of variables between two consecutive iterations, case 22 requires 4992 iterations among the equations, whereas this number for case 25 is 3713 (~25% less). This reduction in computational time per time step is also confirmed by Fig. 6(e) and (f) which demonstrates that with the same number of time steps, the second-order time scheme is generally much less time consuming than its first-order counterpart. Last but not least, with tfds being fixed in cases 20–22, or 23–25, doubling the number of time steps results in less than 15% increase in CPU time. Examination of Table 5 again proves that the issue of coupling between the equations contributes to such a favorable non-linearity, which can also be observed in Fig. 6(e) and (f).

5. Conclusions

A low-cost highly accurate finite volume method was implemented to solve the local mean energy model of non-equilibrium plasmas in a one-dimensional RF configuration. From our numerical experimentations it became apparent that consistent high-order treatment of convection and diffusion fluxes, gradients, boundary conditions and volume integrations is critical in obtaining higher orders of global accuracy, and thus faster rate of convergence to mesh independence and lower computational cost. According to our temporal error analysis, increasing the scheme order for the temporal term results in drastic enhancement of level of accuracy per unit CPU time, and dramatic decrease of CPU time per time step. In brief, when using second-order time scheme in conjunction with fourth-order spatial schemes, lower temporal and spatial resolution, and hence less CPU time, are required to achieve a certain level of accuracy.

Our code is developed for non-uniform meshes and by employing non-orthogonal meshes has the ability to handle two- and three-dimensional problems with realistic complex geometries such as those used in PECVD processes. In such a case, the presented technique with only a moderately high-order correction of the fluxes can overcome the prohibitive cost of lower order computations. Obviously, when the mesh is non-orthogonal, additional interpolation operations are required since points of interpolation polynomials are no longer on mesh lines. Acceleration of the computations becomes crucial also in the problems where chemical reactions are taken into account, or in two-way coupling of dense particle phase with the plasma phase in a particle-laden plasma flow.

Acknowledgments

This work was supported by Grant CBET-0651362 from the US National Science Foundation. John S. Shrimpton would like to thank the EPSRC for funding his advanced research fellowship which permitted a six month visit to UIC during 2006.

Appendix I. Various numerical schemes used in this study to evaluate n_i on the east or west cell faces of a CV, P in Fig. 2, are as follows:

1. First-order upstream approximation,
$$n_i^{(i)}|_e = \begin{cases} n_i|_P & E|_e \geqslant 0 \\ n_i|_E & E|_e < 0 \end{cases}$$
$$n_i^{(h)}|_e - n_i^{(l)}|_e = 0$$
2. Second-order central difference approximation,
$$n_i^{(i)}\Big|_e = \frac{x_E - x_e}{x_E - x_P} n_i\Big|_P + \frac{x_e - x_P}{x_E - x_P} n_i\Big|_E$$
$$n_i^{(h)}\Big|_e - n_i^{(l)}\Big|_e = 0$$

3. Following the flux limiter approach for constructing high-order Total Variation Diminishing (TVD) scheme [46], where the low-order flux is taken to have the form of monotone, first-order upwinding, and the high-order flux to be second-order central differencing, for a non-uniform grid one obtains

$$n_i^{(i)}|_e = \begin{cases} n_i|_P & E|_e \geqslant 0 \\ n_i|_E & E|_e < 0 \end{cases}$$

$$n_i^{(h)}|_e - n_i^{(l)}|_e = \begin{cases} \psi(r_e^+)\frac{x_e - x_P}{x_E - x_P}(n_i|_E - n_i|_P) & E|_e \geqslant 0 \\ \psi(r_e^-)\frac{x_e - x_E}{x_E - x_P}(n_i|_E - n_i|_P) & E|_e < 0 \end{cases}.$$

Thus, TVD schemes use upwinding for calculation of the implicit component of the flux [$n_i^{(i)}|_e$ in Eq. (18)], in conjunction with a limited slope as the explicit component. This implies second-order accuracy in smooth regions (i.e. where the ratio r_e is close to unity). In non-smooth regions, the limiter function is normally designed in such a way to adaptively reduce the influence of the higher-order terms so that the scheme remains conservative. Unfortunately, this increases the first-order upwind contribution, and hence also the numerical dissipation of the gradient. r_e is the ratio of the consecutive gradients in the upstream over the local (at face e) directions, defined as [46],

$$r_e^+ = \frac{(n_i|_P - n_i|_W)/(x_P - x_W)}{(n_i|_E - n_i|_P)/(x_E - x_P)} \qquad E|_e \geqslant 0$$

$$r_e^- = \frac{(n_i|_E - n_i|_{EE})/(x_E - x_{EE})}{(n_i|_P - n_i|_E)/(x_P - x_E)} \qquad E|_e < 0$$

Among the various forms of the limiter function $\psi(r_e)$, we selected Superbee [49] which applies the minimum limiting and maximum steepening possible to remain TVD,

$$\psi(r_e) = \max[0, \min(1, 2r_e), \min(2, r_e)].$$

4. Convection schemes of order greater than 2 use deferred correction method as follows. The implicit part of the flux is defined based on either upstream or central difference scheme, and the explicit component is the difference between the high-order scheme employing Lagrange interpolation polynomials, and the explicit expression for $n_i^{(i)}|_e$. Denoting the nodal values of n_i at N neighboring cell center points x_i (or x_k) by $n_i(x_i)$, and using the Lagrange interpolating polynomial of degree $N-1$ which passes through these N points, the higher order flux at the cell face e is written as [50],

$$n_i^{(h)}|_e = \sum_{i=1}^{N} n_i(x_i) \prod_{k=1,\neq i}^{N} \frac{x_e - x_k}{x_i - x_k}. \tag{19}$$

Provided the interpolation arrays are pre-computed once and prior to the simulation, significant improvements in spatial and global accuracy for very modest additional CPU time overhead are possible.

References

[1] M.A. Lieberman, A.J. Litchenberg, Principles of Plasma Discharges and Materials Processing, first ed., Wiley-Interscience, New York, 1994.
[2] J. Cao, T. Matsoukas, Deposition kinetics on particles in a dusty plasma reactor, J. Appl. Phys. 92 (5) (2002) 2916–2922.
[3] E. Gogolides, H.H. Sawin, Continuum modeling of radio-frequency glow discharges. I. theory and results for electropositive and electronegative gases, J. Appl. Phys. 72 (9) (1992) 3971–3987.
[4] D.B. Graves, Fluid model simulations of a 13.56 MHz rf discharge: Time and space dependence of rates of electron impact excitation, J. Appl. Phys. 62 (1) (1987) 88–94.
[5] S.K. Park, D.J. Economou, Analysis of low-pressure rf glow discharges using a continuum model, J. Appl. Phys. 68 (8) (1990) 3904–3915.
[6] S.K. Park, D.J. Economou, Parametric study of a radio-frequency glow discharge using a continuum model, J. Appl. Phys. 68 (9) (1990) 4888–4890.
[7] Y.H. Oh, N.H. Choi, D.I. Choi, A numerical simulation of rf glow discharge containing an electronegative gas composition, J. Appl. Phys. 67 (7) (1990) 1–12.
[8] A.P. Paranjpe, J.P. McVittie, S.A. Self, Algorithms for numerical simulation of radio-frequency glow discharges, Phys. Review A 41 (12) (1990) 6949–6962.
[9] E. Gogolides, H.H. Sawin, Continuum modeling of radio-frequency glow discharges. II. parametric study and sensitivity analysis, J. Appl. Phys. 72 (9) (1992) 3988–4001.
[10] E. Gogolides, H.H. Sawin, R.A. Brown, Direct calculation of time-periodic states of continuum models of radio-frequency plasmas, Chem. Eng. Sci. 47 (15) (1992) 3839–3855.
[11] D.P. Lymberopolous, D.J. Economou, Fluid simulations of glow discharges: Effect of metastable atoms in argon, J. Appl. Phys. 73 (8) (1993) 4888–4890.
[12] J.D.P. Passchier, W.J. Goedheer, A two-dimensional fluid model for an argon rf discharge, J. Appl. Phys. 74 (6) (1993) 3744–3751.
[13] M. Dalvie, M. Suremdra, G.S. Selwyn, Self-consistent fluid modeling of radio-frequency discharges in two dimensions, Appl. Phys. Lett. 62 (24) (1993) 3207–3209.
[14] M.H. Wilcoxson, V.I. Manousiouthakis, Well-posedness of continuum models for weakly ionized plasmas, IEEE Trans. Plasma Sci. 21 (2) (1993) 213–222.
[15] T.E. Nitschke, D.B. Graves, A comparison of particle in cell and fluid simulations of low-pressure radio-frequency discharges, J. Appl. Phys. 76 (10) (1994) 5646–5660.
[16] J.P. Boeuf, L.C. Pitchford, Two-dimensional model of a capacitively coupled rf discharge and comparisons with experiments in the gaseous electronics conference reference reactor, Phys. Rev. E 51 (2) (1995) 1376–1390.
[17] G.J. Nienhuis, W.J. Goedheer, E.A.G. Hamers, W.G.J.H.M. Van Sark, J. Bezmer, A self-consistent fluid model for radio-frequency discharges in SiH_4-H_2 compared to experiments, J. Appl. Phys. 82 (5) (1997) 2060–2071.
[18] G.J.M. Hagelaar, G.M.W. Kroesen, Speeding up fluid models for gas discharges by implicit treatment of the electron energy source term, J. Comput. Phys. 159 (1) (2000) 1–12.

[19] Y.H. Lin, R.A. Adomaitis, Simulation and model reduction methods for an rf plasma glow discharge, J. Comput. Phys. 171 (2) (2001) 731–752.
[20] G. Salabas, G. Gousset, L.L. Alves, Two-dimensional fluid modelling of charged particle transport in radio-frequency capacitively coupled discharges, Plasma Sources Sci. Technol. 11 (2002) 448–465.
[21] D. Herrebout, A. Bogaerts, M. Yan, R. Gijbels, W. Goedheer, E. Dekempeneer, One-dimensional fluid model for an rf methane plasma of interest in deposition of diamond-like carbon layers, J. Appl. Phys. 90 (2) (2001) 570–579.
[22] A.L. Yarin, B. Rovagnati, F. Mashayek, T. Matsoukas, A reaction model for plasma coating of nanoparticles by amorphous carbon layers, J. Appl. Phys. 99 (6) (2006) 064310-1–064310-12.
[23] J.J. Lowke, K. Davies, Properties of electric discharges sustained by a uniform source of ionization, J. Appl. Phys. 48 (12) (1977) 4991–5000.
[24] J.P. Boeuf, Numerical model of rf glow discharges, Phys. Rev. E 36 (6) (1987) 2782–2792.
[25] J.P. Boeuf, A two-dimensional model of dc glow discharges, J. Appl. Phys. 63 (5) (1988) 1342–1349.
[26] M.S. Barnes, T.J. Colter, M.E. Elta, Large-signal time-domain modeling of low-pressure rf glow discharges, J. Appl. Phys. 61 (1) (1987) 81–89.
[27] S.K. Dhali, P.F. Williams, Two-dimensional studies of streamers in gases, J. Appl. Phys. 62 (12) (1987) 4696–4707.
[28] S.T. Surzhikov, Y.P. Raizer, Two-dimensional structure in a normal glow discharge and diffusion effects in cathode and anode spot formation, High Temp. 26 (3) (1988) 304–310.
[29] N. Spyrou, C. Manassis, Spatio-temporal evolution of a transversally excited electrical discharge in Nitrogen, J. Phys. II France 1 (1991) 1021–1031.
[30] O. Leroy, G. Gousset, L.L. Alves, J. Perrin, J. Jolly, Two-dimensional modelling of SiH_4-H_2 radio-frequency discharges for a-Si:H deposition, Plasma Sources Sci. Technol. 7 (3) (1998) 348–358.
[31] J. Shi, M.G. Kong, Cathode fall characteristics in a dc atmospheric pressure glow discharge, J. Appl. Phys. 94 (9) (2003) 5504–5513.
[32] S. Roy, D. Gaitonde, Radio-frequency induced ionized collisional flow model for application at atmospheric pressures, J. Appl. Phys. 96 (5) (2004) 2476–2481.
[33] S. Roy, B.P. Pandey, J. Poggie, D.V. Gaitonde, Modeling low-pressure collisional plasma sheath with space-charge effect, Phys. Plasmas 10 (6) (2003) 2578–2585.
[34] T. Callebaut, I. Kochetov, Y. Akishev, A. Napartovich, C. Leys, Numerical simulation and experimental study of the corona and glow regime of a negative pin-to-plate discharge in flowing ambient air, Plasma Sources Sci. Technol. 13 (2) (2004) 245–250.
[35] S.T. Surzhikov, J.S. Shang, Two-component plasma model for two-dimensional glow discharge in magnetic field, J. Comp. Phys. 199 (2) (2004) 437–464.
[36] M. Davoudabadi, F. Mashayek, Dust particle dynamics in low-pressure plasma reactor, J. Appl. Phys. 100 (8) (2006) 083302-1–083302-10.
[37] M. Davoudabadi, F. Mashayek, Numerical modeling of dust particles configurations in a cylindrical radio-frequency plasma reactor, Phys. Rev. E 76 (5) (2007) 056405-1–056405-12.
[38] A.L. Ward, Calculations of cathode-fall characteristics, J. Appl. Phys. 33 (9) (1962) 2789–2794.
[39] M.S. Barnes, T.J. Colter, M.E. Elta, A staggered-mesh finite-difference numerical method for solving the transport equations in low-pressure rf glow discharges, J. Comput. Phys. 77 (1) (1988) 53–72.
[40] E.P. Hammond, K. Mahesh, P. Moin, A numerical method to simulate radio-frequency plasma discharges, J. Comput. Phys. 176 (2) (2002) 402–429.
[41] A. Fiala, L.C. Pitchford, J.P. Boeuf, Two-dimensional, hybrid model of low-pressure glow discharges, Phys. Rev. E 49 (6) (1994) 5607–5622.
[42] G.L. Huppert, H.H. Sawin, R.A. Brown, Spectral element analysis of radio-frequency glow discharge, Chem. Eng. Sci. 49 (10) (1994) 1601–1611.
[43] P.K. Kholsa, S.G. Rubin, A diagonally dominant second-order accurate implicit scheme, Comput. Fluids 2 (1974) 207–209.
[44] J.H. Ferziger, M. Peric, Computational Methods for Fluid Dynamics, third ed., Springer, New York, 2002.
[45] G.J.M. Hagelaar, F.J. de Hoog, G.M.W. Kroesen, Boundary conditions in fluid models of gas discharges, Phys. Rev. E 62 (1) (2000) 1452–1454.
[46] E.F. Toro, Riemann Solvers and Numerical Methods for Fluid Dynamics, second ed., Springer, New York, 1999.
[47] W.J. Goedheer, (private communication).
[48] L.V. Ballestra, R. Sacco, Numerical problems in semiconductor simulation using the hydrodynamic model: a second-order finite difference scheme, J. Comput. Phys. 195 (1) (2004) 320–340.
[49] P.L. Roe, Characteristic-based schemes for the Euler equations, Ann. Rev. Fluid Mech. 18 (1986) 337–365.
[50] M. Abramowitz, I.A. Stegun, Handbook of Mathematical Functions with Formulas, Graphs, and Mathematical Tables, ninth ed., Dover, New York, 1964.